Struct Chem (2013) 24:955–965
DOI 10.1007/s11224-013-0221-5

ORIGINAL RESEARCH

Experimental and in silico characterization of a biologically active inosose

Venerando Pistarà · Giuseppe M. Lombardo · Antonio Rescifina · Alessia Bacchi · Felicia D'Andrea · Francesco Punzo

Received: 30 November 2012 / Accepted: 23 January 2013 / Published online: 8 February 2013

Abstract Inositols have been recently reported to show a biological activity as inhibitors of both glycosidase and amyloid-β protein. After having harvested good crystals suitable for single crystal X-ray diffraction, we performed a comparison with the data inferred by means of a molecular dynamics simulation, based on the use of an appropriate Force Field coupled to the most performing charging scheme. This approach allowed a detailed analysis extended to ultra-fine details, such as atomic displacement parameters. It confirmed the good validity of a robust approach already tested by us in previous studies. A NMR analysis of the molecule in solution was also carried out, to compare the structural findings suggested by the X-ray analysis with the ones in solution and avoid confining them to the solid-state. In this framework, we investigated the above-mentioned inhibiting activity of a class of inososes, by means of a molecular docking investigation, which proved the suggested validity of the studied compound as inhibitor of the α-glucosidase.

Keywords Inososes · Glycosidase inhibitors · Docking · Molecular dynamics simulation · X-ray structural analysis · Atomic displacement parameters

Introduction

Cyclitols are cycloalkanes with one hydroxyl group on each ring atom and other closely related compounds containing a C=C double bond in the ring such as amino, alkyl or halogen substituents. Among these, inositols (hexahydroxycyclohexanes) are an interesting group of carbocyclic sugar analogs, which keep attracting a great deal of attention due to the ubiquitous presence of their derivatives in living cells and their implication in biological phenomena [1–4]. Among them, *myo*-inositol is the most abundant of the nine possible stereoisomers and it plays a very important role in cellular signal transduction acting as second messenger [1–4]. D-*chiro*-inositol is a drug candidate for the treatment of type 2 diabetes [5] and polycystic ovary syndrome [6]. L-*chiro*-inositol is a potential antidiabetic compound [5]. *Neo*-inositol phosphates have been isolated from both mammalian tissue [7] and parasitic amoebas [8], while *scyllo*-inositol from human brain [9], as well as from plants [10]. *Epi*-inositol recently has been evaluated as a potential anti-depressant drug that could interact with lithium ions and *myo*-inositol receptors in the brain [11, 12].

Even the corresponding ketones of inositols, the so called inososes, have been found in small portions in mammalian tissues [13] and in *Streptomices griseus* [14], like the common *myo*-inosose (Fig. 1). Furthermore, these

Dedicated to Professor Aldo Domenicano on the occasion of his 75th birthday.

V. Pistarà · G. M. Lombardo · A. Rescifina (✉) · F. Punzo (✉)
Divisione Chimica, Dipartimento di Scienze del Farmaco, Università degli Studi di Catania, Viale Andrea Doria 6, 95125 Catania, Italy
e-mail: arescifina@unict.it

F. Punzo
e-mail: fpunzo@unict.it

A. Bacchi
Dipartimento di Chimica Generale ed Inorganica, Chimica Analitica, Chimica Fisica, Università degli Studi di Parma, Parco Area delle Scienze 17/A, 43124 Parma, Italy

F. D'Andrea
Dipartimento di Scienze Farmaceutiche, Università degli Studi di Pisa, Via Bonanno 33, 56126 Pisa, Italy

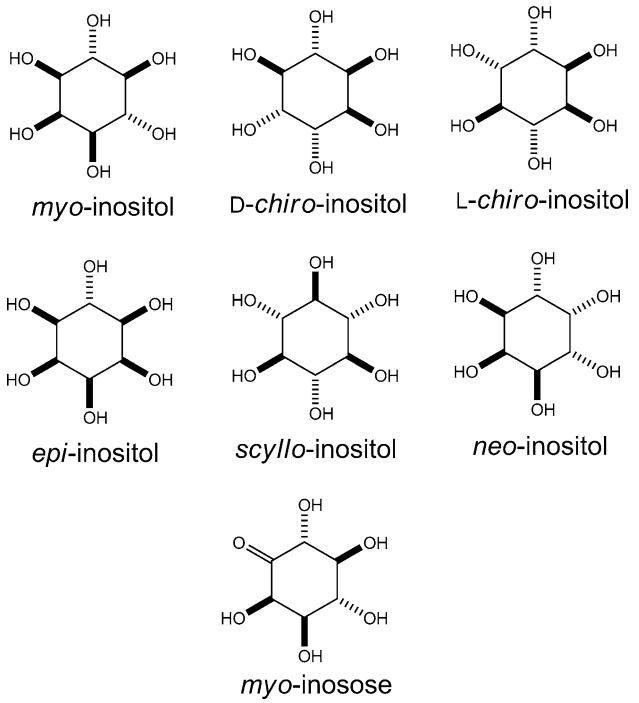

Fig. 1 Chemical structures of cited cyclitols

compounds are useful intermediates for cyclitol synthesis in nature, as proposed in the Kiely's biomimetic synthesis of *myo*-inositol from D-*xylo*-hexos-5-ulose [15].

In a recent study about the amyloid-β (Aβ) protein [16], a key mediator of Alzheimer's disease pathology, the effects of the inositol and inosose stereoisomers as potential therapeutic agent for amyloid disorders have been reported. These compounds exhibit stereospecific inhibition of Aβ aggregation in vitro and in vivo, with significant decreases in Aβ40 and Aβ42 levels, vascular amyloid levels, plaques size and area that were observed by the authors.

In the past years, starting from unsatutared derivatives of galactopyranosides, some of us studied the synthesis of 1,5-dicarbonyl sugars [17–21], which are key intermediates for the synthesis of high valued-added compounds such as gabosines [22], cyclitols [23, 24], and azasugar [25]. Few years ago, following the Kiely's biomimetic synthesis [15], was developed a useful synthetic procedure [23], that, starting from methyl β-D-galactopyranoside **1**, produced the inosose derivative **3** via the diazabicycloundecene (DBU)-mediated intramolecular aldol condensation of l-*arabino*-aldohexos-5-ulose **2**. Finally, the catalytic debenzylation followed by the reduction of inosose gave rise to *epi*-inositol **4** as described in Scheme 1 [23]. When the aldol condensation was carried out with a catalytic amount of NaOH in aqueous methanol, the formation of inosose **3** was not stereospecific and a second inosose, **5**, was identified as minor product (about 2:1 ratio, 70 % overall yield), thus indicating that the solvent and/or the base promoter play a specific role in the reaction stereochemical outcome. At that time the structure of this second inosose remained under investigation.

Nowadays, having obtained good crystals of **5**, suitable for X-ray diffraction, we report the complete characterization of inosose **5** by means of X-ray single crystal diffraction and of both **5** and **6** with NMR. Moreover, we have carried out a molecular dynamics (MD) simulation that, combined and compared with the X-ray diffraction data of the same condensed phase, was able to provide structural information that are otherwise inaccessible [26–30].

Finally, as it was recently reported that several inositols and their derivatives act as inhibitors of glycosidases, we tried to determine whether compounds **5** and **6** and their enantiomers, *ent*-**5** and *ent*-**6**, are able to bind effectively with the active site of the N-terminal catalytic subunit of human maltase-glucoamylase (NtMGAM).

Results and discussion

X-ray crystallography

The molecular structure of **5** is reported in Fig. 2 along with its labeling scheme. A ring puckering analysis—i.e., Cremer and Pople (C&P) analysis [31]—was performed on the six-membered ring C1–C2–C3–C4–C5–C6 (see Table 1 for ring nomenclature), actually the only suitable ring for this analysis, being the other two aromatic and therefore planar. The representation of the ring puckering can be performed by means of a single amplitude-phase pair—q2 and ϕ2, 0.019(2) Å and 27(6)°, respectively—as well as a single puckering coordinate q3 (0.577(2) Å) in the case of six-membered rings, where the puckering degrees of freedom are three. The same results can be obtained using spherical coordinates, Q, θ, and ϕ as shown in Ref. [32].

The conformation analysis allows the assignment of a typical chair (C) conformation to the above-mentioned ring [33].

The search for hydrogen bonds evidenced the existence of a complex and vast network of interactions reported in Table 2.

Based on distance criteria, whereby the donor…acceptor distance is less the sum of the Van der Waals radii, both intra- and intermolecular hydrogen bonds are present in the structure, as well as strong (O–H···O) and weak (C–H···O) ones, where the strength depends on the electronegativity of the donor. The weak intermolecular C–H···O interactions assist the packing in the formation of hydrogen bonded chains along the a axis, already sustained by the stronger O–H···O interactions (O3–H···O6 and O6–H···O3,

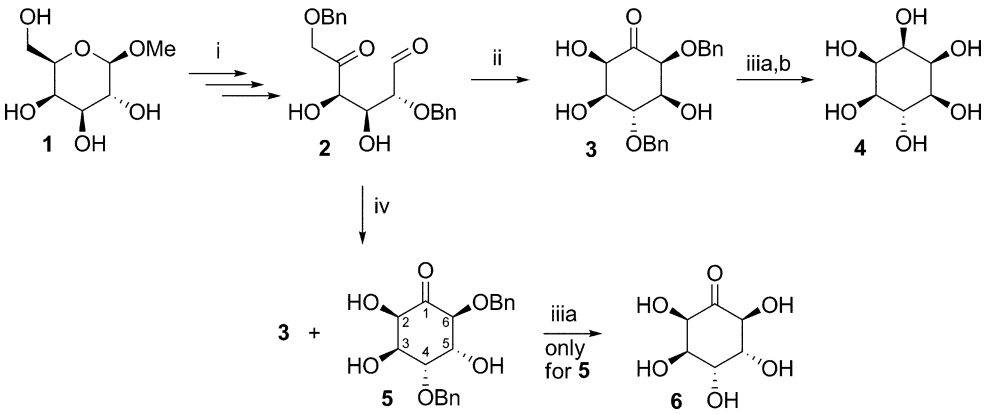

Scheme 1 Synthetic pathway for inososes **5** and **6**. (*i*) Ref. [17]; (*ii*) DBU, toluene, rt; (*iii*) *a* H_2–Pd(C), MeOH; *b* Ni/Raney/H_2, MeOH; (*iv*) NaOH, MeOH/H_2O

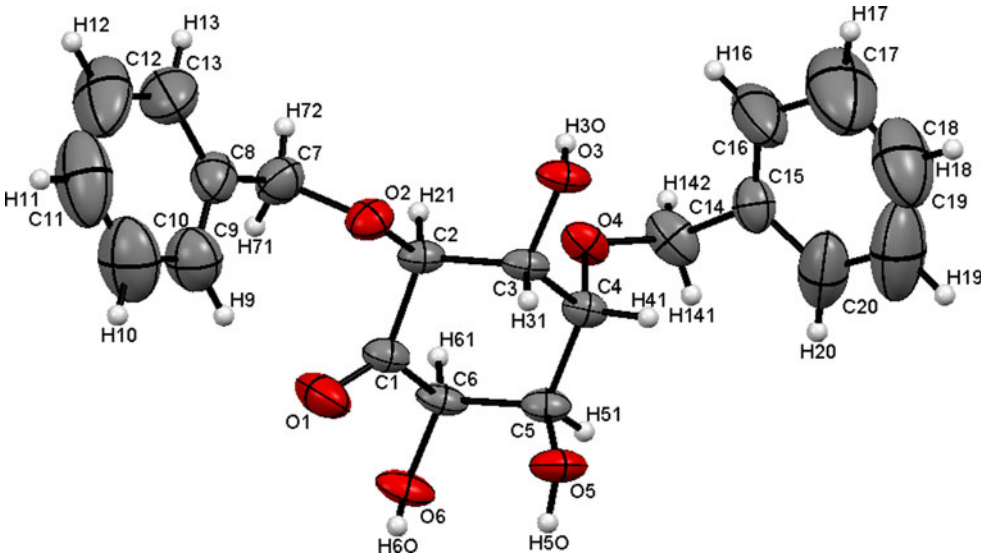

Fig. 2 Molecular structure and labeling of **5**. Thermal displacement ellipsoids are drawn at the 50 % probability level while hydrogen atoms are represented as *spheres* of arbitrary radius

Table 1 Compact nomenclature for the center of gravity (Cg) of the rings in **5**

	5
Cg(1)	C1–C2–C3–C4–C5–C6
Cg(2)	C8–C9–C10–C11–C12–C13
Cg(3)	C15–C16–C17–C18–C19–C20

Table 2). The ancillary role of weak CH···O hydrogen bonds in supramolecular recognition is widely known both in the crystal engineering and macromolecular crystallography [34, 35]. Interestingly, there is evidence of two bifurcated hydrogen bonds [36], involving O3–H30···O6 and O5–H50···O3, which provide a further aid to the overall stabilization of the structure. In this framework, it could not be neglected the role of the several non-covalent π–π stacking and T-shaped interactions present and reported in Table 3 [37–41].

The crystal is organized in two-dimensional layers built in the bc plane by strong hydrogen bonds, and then assembled in the third direction, along the *a* axis, by weak lipophilic CH···π interactions (Fig. 3). A characteristic zigzag motif is evidenced. **5** Crystallized with a quite low packing index [42]. Four small voids are present in the structure although they are not suitable for a possible inclusion of solvent molecules. In fact the total potential solvent volume is 37.4 $Å^3$ which represents only the 2.1 % of the total cell volume.

Molecular dynamics

The analysis of the internal molecular fluctuations, which are directly comparable to those obtained from diffraction data, provides a tool for validating the simulated trajectory [43]. The description of the various interactions between all the atoms of the considered system, a prerequisite needed by any correctly performed MD simulation, is usually done either by the quantum mechanical (QM) scheme, as introduced by Car and Parrinello [44], or by classical empirical force fields (FF). As QM driven MD scheme are quite computationally expensive, whenever QM effects can be neglected, empirical FF are preferred [45]. In previous works we performed a

Table 2 Hydrogen-bonds list

Hydrogen-bond geometry (Å, °)					
D–H···A	D–H	H···A	D···A	D–H···A	H bond classification
O3–H30···O4	0.72 (3)	2.51 (3)	2.785 (3)	105 (2)	Intra and bifurcated
O3–H30···O6i	0.72 (3)	2.18 (3)	2.843 (2)	154 (3)	Bifurcated
O5–H50···O2ii	0.83 (4)	2.24 (4)	3.009 (2)	155 (3)	Bifurcated
O5–H50···O3ii	0.83 (4)	2.47 (4)	3.070 (2)	130 (3)	Bifurcated
O6–H60···O3ii	0.86 (4)	1.97 (4)	2.818 (2)	170 (3)	
C6–H61···O5iii	1.02 (3)	2.51 (2)	3.323 (3)	136.4 (17)	
C7–H71···O1	0.97 (3)	2.58 (3)	3.139 (3)	116.9 (18)	Intra

Symmetry codes: (i) $-1-x$, $\frac{1}{2}+y$, $-\frac{1}{2}-z$; (ii) $1+x$, y, z; (iii) $-2-x$, $-\frac{1}{2}+y$, $-\frac{1}{2}-z$. Full geometry parameters are reported. D identifies the donor, A the acceptor, and H the hydrogen atom involved. Standard uncertainties (s.u.s) are reported in parentheses for all distances (see "Experimental" section for details). The last two entries are weak intramolecular hydrogen bonds [34]. H bond classification has been done on the basis of Ref. [36]

Table 3 Selected π–π–stacking non-covalent interactions between aromatic rings in **5**

Centroid (I)···centroid (J)	Distance (Å)	Angle (°)	Slippage (Å)
Cg (2)···Cg (2)i,ii	5.060 (3)	0	3.622
Cg (2)···Cg (2)iii	5.222 (2)	89	–
Cg (3)···Cg (3)i	5.061 (4)	0	3.500
Cg (3)···Cg (3)ii	5.059 (4)	0	3.499
Cg (3)···Cg (3)iv	5.357 (3)	88	–

Symmetry codes: (i) $-1+x$, y, z; (ii) $1+x$, y, z; (iii) $\frac{1}{2}+x$, $-\frac{1}{2}-y$, $-1-z$; (iv) $\frac{1}{2}+x$, $-\frac{1}{2}-y$, $-z$. Distances and relative s.u.s are measured in Å and angles in (°) between adjacent centroids (Cg)

thorough comparison of QM and empirical FF applied to the study of small organic molecules [46, 47]. The reported results evidenced how the chosen empiric FF best reproduced, even if compared to the QM ones, the ab initio H-bonding and stacking stabilization energies.

This task was accomplished using the AMBER FF [48], with the Cornell et al. parameterization, as implemented in the Discover module of the Materials Studio package of Accelrys. Moreover, to validate the NPT (isothermal and isobaric) MD simulations from these trajectories, we calculated the anisotropic displacement parameters (adps)—or temperature factors—to illustrate the atom's thermal motions relative orientation and compared them to the ones inferred by means of the X-ray analysis.

In order to model the crystal structure without assuming any particular symmetry, the original $P2_12_12_1$ cell was transformed in a triclinic P1 one with all the symmetry related atoms, together with the cell parameters, to be independent variables during a NPT ensemble simulation.

We proceeded by evaluating expanded structure models, with a $5 \times 2 \times 1$ supercell, i.e., built by replicating the unit cells five times along *a* and two times along *b* to withdraw border effects introduced by the short periodic boundary conditions (PBC) of the single unit cell. The starting models were based on the experimental cell and the resulting MD trajectories embed cell parameters, which now are fluctuating around the starting values without

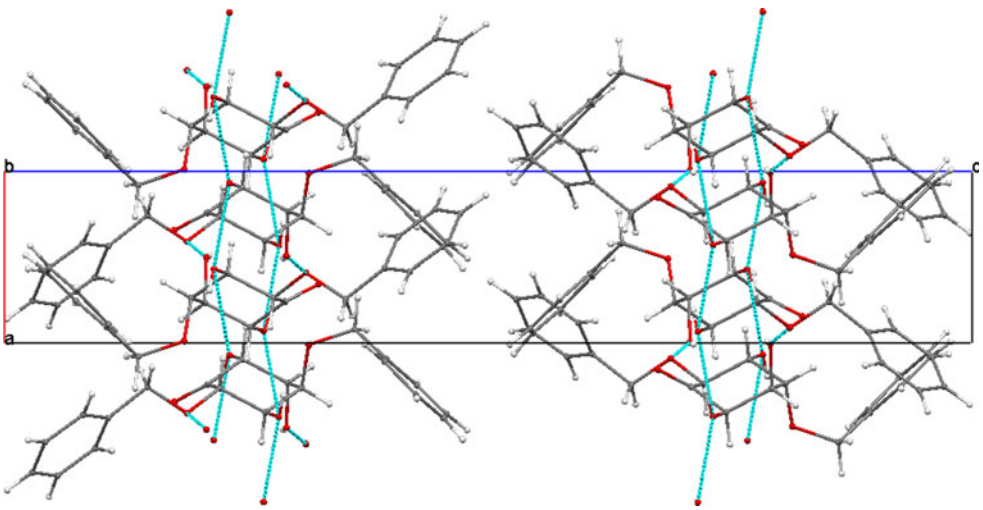

Fig. 3 Crystal packing of **5**, projected down the *a* axis. Hydrogen bonds are reported as a *dashed line*

evidencing any particular phase transition, thus indicating that the considered structure could be considered stable.

Furthermore, we tried to check whether the original AMBER FF charges scheme adequately account for the experimental structure. In order to perform this task, a step was made toward the definition of a suitable atomic charge distribution. In previous works only the charge equilibration (Qeq) scheme [46, 47], which bases its values on atoms electronegativity differences and relative distances, properly kept the MD simulation cell parameters with the smallest differences with respect to the X-ray ones. However, as described in Fig. 4, the best results were achieved by the direct use of the AMBER embedded setup. The analysis of the above-mentioned figure allows the direct qualitative evaluation of the closer correspondence of the AMBER inferred adps (left) with respect to the ones calculated with the Qeq charging scheme (right), as compared to the ones inferred from the experimental X-ray data (middle). Interestingly, not only the size of the adps could be considered very similar, but also their preferential elongation in a given direction is resembled.

In Fig. 5 we reported a quantitative comparison among the differently inferred adps values (AMBER, Qeq, X-ray inferred), and the ones calculated basing our simulation on the restrain of the symmetry equivalent fragments in the unit cell, i.e., not relaxing but instead keeping the symmetry. It is evident that the latter values are quite smaller than the other ones which, qualitatively show very similar trends. An explanation for this behavior could be found by considering the presence of symmetry constraints which forbid the free and independent movement of each fragment present in the unit cell, thus forcing symmetry-related fragments to oscillate with opposite phases. The result of this process is the overall dumping of the libration of each single atom, evidenced by smaller adps, as reported in the above-mentioned figure. In the light of this reasoning, it is not possible to claim that the calculated adps are systematically smaller than the X-ray inferred ones, as often reported in literature, as their sizes and shapes are heavily affected by the way the calculation is carried out—i.e., relaxing or not the symmetric constraints [49, 50].

Moreover, there is an expected and constant trend that could be inferred by a visual inspection of the adps layout obtained by the superimposition of the experimental data (shadowed) to the simulated ones (solid) as reported in Fig. 6: the ones belonging to the benzene rings are experiencing greater fluctuations around their equilibrium positions than the ones of the central nonaromatic ring, and among them, the more external ones show this behavior even in a more exasperated manner. This is clearly due to their increasing distance from the center of mass of the molecule, and this behavior is well-simulated by the computational

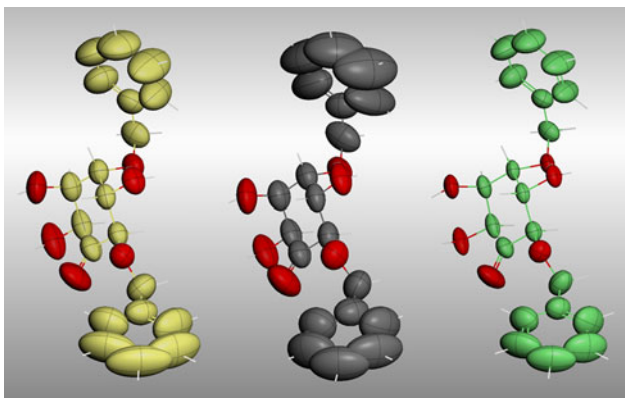

Fig. 4 Visual comparison among asymmetric units of **5** and their relative adps, as inferred MD simulation based on the original AMBER setup (*left*), by X-ray single crystal diffraction (*middle*) and AMBER setup with Qeq charging scheme (*right*)

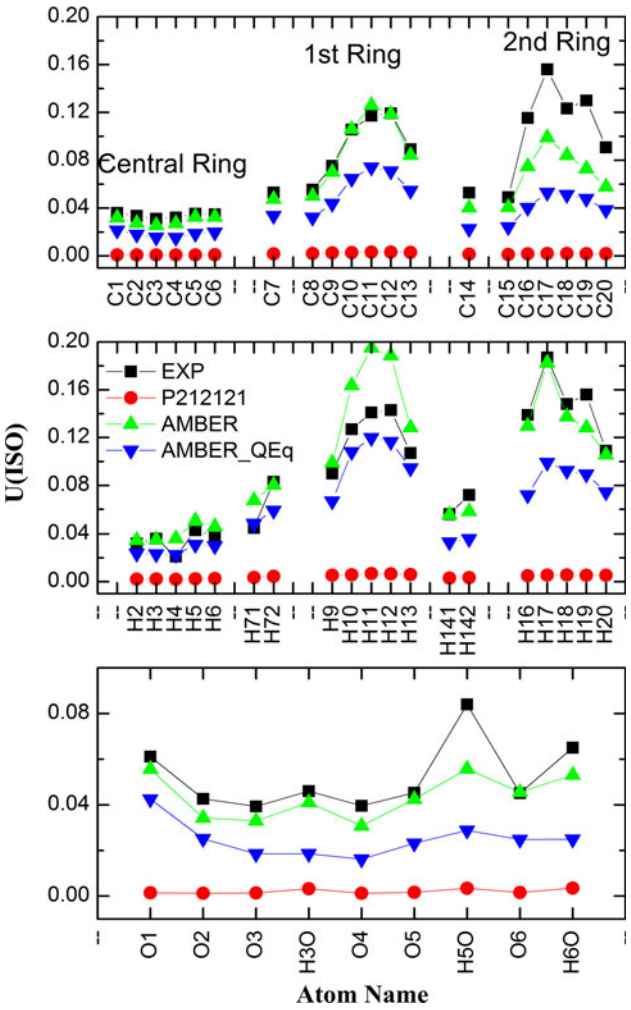

Fig. 5 Uequiv (Uiso for hydrogen atoms) trends comparison among the X-ray experimental values and the MD ones, the latter calculated with the standard AMBER setup, AMBER with Qeq charging scheme and without relaxing the symmetry, respectively. Carbon, hydrogen, and oxygen atoms, are reported in the *upper*, in the *middle* and in the *lower* part of the figure, respectively

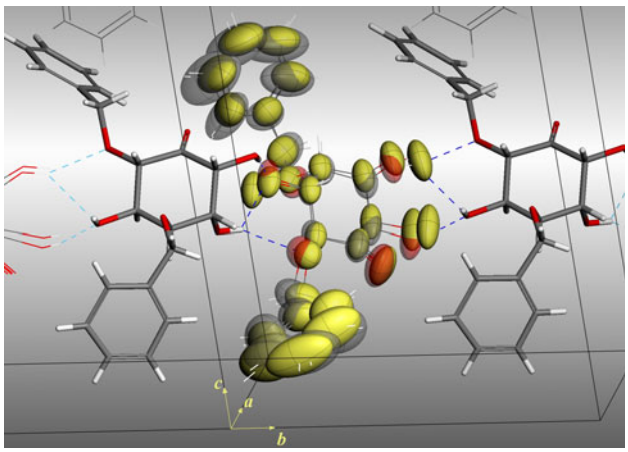

Fig. 6 Superimposition of the experimental crystal packing with the model I MD averaged one. The experimental anisotropic thermal factors are shown (*shadowed*) and compared with the MD calculated ones (*solid*). The agreement in the anisotropic thermal factors is extended to the whole MD calculated super-cell and not only confined to the single unit fragment

results which are in very good agreement, once again, with the X-ray experimental data. Moreover, the accordance in the anisotropic thermal factors is extended to the whole MD calculated super-cell and not only confined to the single unit fragment. However, taking into account that it is well-known that the overall X-ray low ability to univocally resolve hydrogen atoms' position, the MD simulation can produce a good insight to their relative adps layout. As already commented in Table 2, a complex hydrogen-bond network is present; the adp analysis of the hydrogen atoms involved in different type of hydrogen bonds—i.e., linear and bifurcated ones—seems to confirm that the X-ray inferred values, although not always trustable in principle, are in very good agreement with the simulated ones, especially with the values resulted from the AMBER-based simulation (Figs. 5, 6). The agreement is evident both in the trends and in each atom's value. The inspection of the adps layout, for what concerns hydrogen atoms, can be source of other cues. In fact, a preferential direction of elongation of each adp can be considered sign of a directional constrain: the comparison between the experimental and computed data can therefore highlight potential details hidden to the X-ray analysis. At variance with previous works where the differences between calculated and experimental adp values evidenced an underestimation of the weight ascribed by X-ray analysis to the hydrogen bonding [46, 47], the present analysis was not able to spot any substantial difference. This is confirmed by the analysis of Fig. 6, where adps belonging to H30 and H50—the two hydrogen atoms involved in a bifurcated hydrogen bond—as well as the one regarding H60—to mention only the intermolecular hydrogen bonds—show no appreciable differences even by a direct superimposition of the calculated and experimental adp values.

Table 4 Calculated binding energies and inhibition constants to catalytic site of NtMGAM for compounds **5** and **6**, their enantiomers and miglitol

Ligand	ΔG_{Bind} calcd. (kcal/mol)	K_i calcd. (μM)
5	−6.0	36.9
ent-**5**	−6.3	22.8
6	−3.7	2,030
ent-**6**	−3.6	2,110
Miglitol[a]	−8.3	0.8[b]

[a] With nitrogen azasugar protonated in equatorial

[b] From Ref. [25]; exp. 1.0 from Ref. [57]

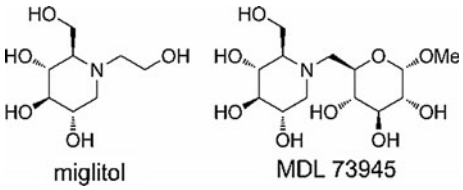

Fig. 7 α-D-Glucosidase inhibitors

It is worth analyzing even the good agreement between the computed and experimental bond distances. However, among many very similar calculated and experimental distances, there is actually an overall tendency to overestimate the bonds involving hydrogen atoms when comparing the simulated data to the experimental ones. This is probably due to the lack of precision in the hydrogen determination—i.e., their position—embedded in the X-ray measurement and not to a MD artifact. In fact, as specified in the experimental section, by following a quite standard operating procedure, hydrogen atoms attached to oxygens, were located in a difference Fourier map and refined isotropically while the other ones bound to carbon were refined using a riding model. This is another evidence of how the comparison with the simulated structure allows an assessed comment on some features of the X-ray one.

NMR studies

The 1D and 2D (NOE, COSY and HETCOR) NMR experiments are in agreement with the X-ray results, confirming the absolute stereochemistry inferred by the solid-state. For what concerns the conformation of the cyclohexanone ring, NMR results showed that there is a little distortion as compared to that evidenced by the solid-state analysis. As a consequence, in the inosose **5** the H2 proton appears as a double doublet (4.31 ppm) with a large $J_{ax/ax}$ (9.5 Hz) coupling with the adjacent H3 and a small $J_{ax/ax}$ (1.5 Hz) with H6 proton, whereas H4 proton

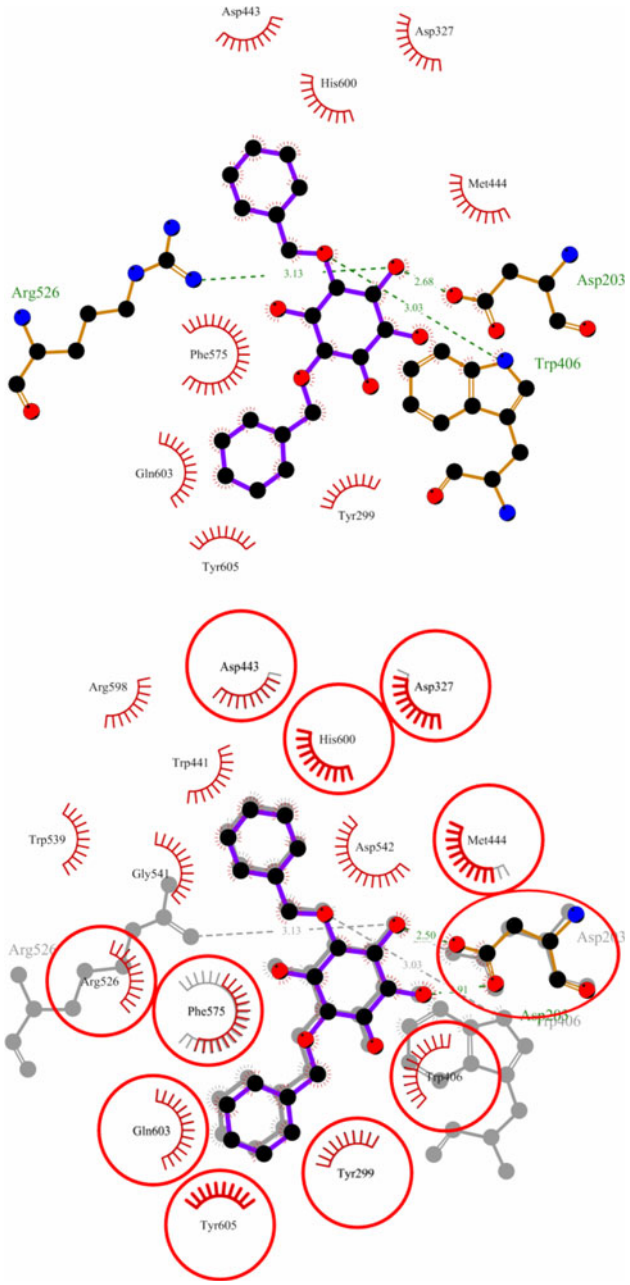

Fig. 8 2D Schematic view of hydrogen bonds and hydrophobic interactions for **5** (*upper*) and its overlap with *ent*-**5** (*down*) docked in NtMGAM, prepared with LigPlot$^+$ [61]. The *circles* indicate common interactions

(3.93 ppm) shows a small *trans* di-equatorial coupling (3.8 Hz) with the H5 one (4.22 ppm) and a *cis*-axial/equatorial disposition with the H3 (3.93 ppm, 4.0 Hz). Although these coupling constants agree with the absolute configuration, in solution they are consistent with a small variation in the dihedral angles, especially for the axial benzylic substituent at C4, which appears as in a quasi-axial conformation, producing a distortion of the classic chair conformation.

Molecular docking

Recently it has been demonstrated that several inositols and their derivatives act as inhibitors of glycosidases [51–56]. It is therefore plausible that the derivatives **5** and **6** may present a similar activity. Thus, we conducted a series of studies of molecular docking to determine whether the subject compounds and their enantiomers, *ent*-**5** and *ent*-**6**, are able to bind effectively with the active site of the *N*-terminal catalytic subunit of human maltase-glucoamylase (NtMGAM). The 3D X-ray crystal structure of NtMGAM domain–miglitol complex [57], was retrieved from the Protein Data Bank [58] and processed, as previously reported [25], following a tested protocol [59].

The obtained results, reported in Table 4, show that derivative *ent*-**5** has the best activity among the studied compounds with an in silico inhibition constant of 22.8 μM, whereas its enantiomer is slightly less efficient. The unprotected compounds **6** are one hundreds of times less active of miglitol, chosen as reference, and then practically useless as drugs. On the contrary, compounds **5** are only about twenty times less active.

Regarding the structure–activity relationships, it is evident that the relative simplification of compounds **6** respect to the miglitol (Fig. 7) and, especially, the absence of a protonable atom, at physiological pH, such the nitrogen one, that engage an hydrogen bond with the Asp443 in the catalytic residue, essential for the inhibitory activity [60], preclude a strong interaction with the enzyme. Vice versa, the presence of the two benzyl groups allow a more adequate filling of the catalytic pocket establishing, at the same time, an extensive hydrophobic interactions network (Fig. 8). Moreover, the benzyl moiety at O4 takes the place of the miglitol, in the catalytic residue, constraining the inosose ring to occupy the +1 site, similarly to what happens with the second glycosidic ring of the MDL 73945, one of the leader α-D-glucosidase inhibitors derived from miglitol (Fig. 7).

Finally, the major activity of compound *ent*-**5** with respect to **5** is due to more extended hydrophobic interactions, as shown in the lower part of Fig. 8.

Conclusions

In this study, we carried out a thorough characterization of **5** not only for what concerns the solid-state but also in solution. The X-ray single crystal structure was the starting point for a detailed comparison, performed by means of a molecular dynamics simulation, that not only confirmed the X-ray inferred experimental data, but also allowed a precise analysis of other structural features which are not directly accessible by the traditional experimental

approach. This was done carrying out a qualitative and quantitative adp analysis, extended to the hydrogen atoms, i.e., one of the known Achille's heel in the X-ray structural determination. It allowed a direct validation of the proposed interpretation of what evidenced by X-rays validating, at difference with previous works the landscape already depicted by the experimental analysis [46, 47]. Moreover, this study confirmed that the magnitude of the calculated adps is strongly affected by the way their simulation is performed i.e., among other things, whether symmetry constraints are released or not. On the other hand, the NMR analysis confirmed, although with a slight variation due to the greater flexibility experienced by the molecule in solution, the peculiarities highlighted by the solid-state analysis. The so inferred structural evidences were joined with the evaluation of the inhibiting activity of **5**, which showed good potentialities, as checked by his docking capabilities.

Experimental

Melting points were determined with a Kofler hot-stage apparatus and are uncorrected. Optical rotations were measured on a Perkin-Elmer 241 polarimeter at 20 ± 2 °C. All reactions were followed by TLC on a Kieselgel 60 F254 with detection by UV light and/or with ethanolic 10 % sulfuric acid. Kieselgel 60 was used for column and flash chromatography (E. Merck, 70–230 and 230–400 mesh, respectively). ^{1}H NMR spectra were recorded with a Varian VnmrJ instrument at 500 MHz in the stated solvent (Me_4Si was used as the internal standard). ^{13}C NMR spectra were recorded at 50 MHz. Assignments were made, when possible, with the aid of DEPT experiments, for comparison with values for known compounds. High-resolution mass spectra were recorded on a VG ZAB-2SE double focusing magnetic sector mass spectrometer operating at 70 eV. The hydrogenation were performed with a Parr apparatus. Solvents were dried by distillation according to standard procedure [62], and stored over 4 Å molecular sieves activated for at least 24 h at 400 °C. Na_2SO_4 was used as drying agent for solutions.

Good quality crystals were obtained by dissolving **5** in a test tube with acetonitrile and adding few drops of water. The solution was sealed and stored at 4 °C. After several weeks some prismatic colorless crystals were harvested.

Chemistry

*Synthesis of inososes **3** and **5***

To a solution of EtOH/H_2O 9:1 (5 mL) containing the dicarbonyl compound **2** (107.5 mg, 0.3 mmol), was added a 0.005 M NaOH hydroalcoholic solution (2 mL) and the resulted mixture was stirred for 2 h. At the end of the reaction the solvent was removed at reduced pressure and the residue was extracted with CH_2Cl_2 (3 × 5 mL). The combined organic layers were dried over Na_2SO_4, filtered and evaporated at reduced pressure. The resulting crude was purified by flash chromatography (cyclohexane/ethyl acetate, 6:4), affording inososes **3** and **5** in a 2:1 ratio (70 % overall yield).

*2D-2,4-Di-O-benzyl-(2,3,6/4,5)-pentahydroxycyclohexanone **5***: yield 24 %, 26 mg; mp 169–171 °C, colorless crystals from acetonitrile; $[\alpha]_D^{25} = -51$ ($c = 0.31$, $CHCl_3$). ν_{max} (KBr) 3471, 3450, 3382, 1725, 1624 cm^{-1}. ^{1}H NMR (500 MHz, $CDCl_3$, 27 °C): δ 7.25–7.47 (m, 10H, phenyl H), 4.77–4.68 (AB system, 2H, $J = 11.5$ Hz, CH_2Ph), 4.76–4.48 (AB system, 2H, $J = 11.5$ Hz, CH_2Ph), 4.49 (dd, 1H, $J = 1.5$, 4.0 Hz, H6), 4.31 (dd, 1H, $J = 1.5$, 9.5 Hz, H2), 4.22 (t, 1H, $J = 3.8$ Hz, H5), 3.93 (dd, 1H, $J = 4.0$, 9.5 Hz, H3), 3.92 (dd, 1H, $J = 3.8$, 4.0, H4); ^{13}C NMR (125 MHz, CDCl3, 27 °C): δ 207.5 (C=O), 139.3 (phenyl C), 138.8 (phenyl C), 129.3, 129.2, 129.0, 128.8 and 128.7 (phenyl CH), 83.7 (C2), 79.6 (C4), 74.9 (C6), 74.4 (CH_2Ph), 73.7 (CH_2Ph), 73.4 (C3), 71.9 (C5). Anal. calcd. for $C_{20}H_{22}O_6$: C 67.03, H 6.29 %; found C 67.19, H 6.31 %.

*Debenzylation of **5***

To a solution of compound **5** (26 mg 0.07 mmol) in MeOH (2 mL) was added a spatula tip of 10 % Pd/C and the suspension was set shaken on a Parr apparatus under hydrogen (90 psi) for 24 h. The reaction mixture was filtered through Celite and the filtrate was evaporated at reduced pressure, affording the pure debenzylated compound **6**.

*2D-2,3,6/4,5)-Pentahydroxycyclohexanone **6***: yield 95 % 11.8 mg; colorless crystals from water/2-propanol; mp 195–197 °C; $[\alpha]_D^{25} = -68$ ($c = 0.5$, H_2O). ν_{max} (KBr) 3665, 2917, 1734, 1563 cm^{-1}. ^{1}H NMR (200 MHz, D_2O, 27 °C): δ 4.62 (dd, 1H, $J = 1.3$, 3.6 Hz, H2), 4.39 (dd, 1H, $J = 1.3$, 10.2 Hz, H6), 4.16 (dd, 1H, $J = 3.6$, 3.9 Hz, H3), 4.05 (dd, 1H, $J = 3.3$, 3.9 Hz, H4), 3.73 (dd, 1H, $J = 3.3$, 10.2 Hz, H5); ^{13}C NMR (50 MHz, D_2O, 27 °C): δ 208.0 (C=O), 75.2, 73.2, 73.1, 72.9, 70.3. Anal. calcd. for $C_6H_{10}O_6$: C 40.63, H 5.66 %; found C 40.69, H 5.64 %.

Methods

X-ray crystallography

5 Shows a $P2_12_12_1$ orthorhombic unit cell with $a = 5.0600(4)$ Å, $b = 12.6478(9)$ Å, $c = 28.567(2)$ Å, R being 5.09 %. Although Friedel pairs were not merged, the high s.u. value associated to the—meaningless—Flack

parameter (−0.7 and 12, respectively), coupled with the use of Mo Kα, suggested that experimental data did not support the determination of the absolute configuration of the molecule. This issue has been ascribed to twinning effects that may alter the intensities distribution. However, it was assigned by comparison with a reference molecule of known absolute configuration.

An unusual C atoms thermal displacement parameter (U_{eq}) ratio, confirmed by the MD inferred data, is the result of the comparison between carbons having a very different mobility. This is evidenced by the above or below average U_{eq} values of C17, C12, and C19 on one hand and C8, C15, and C18 on the other. The failure in the Hirshfeld rigid-bond test difference [63] for both C18–C19 bonds is due to some disorder still present in the structure after modeling and, as it is associated with the s.u.; it could be the result of over refinement. The search for possible solvent accessible voids was performed using the VOID algorithm setting a grid of 0.20 Å and a probe radius of 1.20 Å [64]. The H atoms were all located in a difference map, but those attached to aromatic carbon atoms were repositioned geometrically with fixed bond lengths and angles to regularize their geometry (C–H in the range 0.93–0.98 Å) and Uiso (H) (in the range 1.2–1.5 times U_{eq} of the parent atom), riding on their carrier atoms. All the other hydrogen atoms were refined isotropically without restraints. The data collection was performed at 293 K, and the strategy used aimed to achieve a complete data set to $2\theta = 55°$. Some higher angle data were collected in the process and these have been included in the refinement.

The following software have been used for data treatment and collection: SAINT-Plus [65] and SADABS [66]. Mercury was used for molecular graphics [67].

Atomic displacement parameters

For the detailed and complete description of the calculation of adps see Ref. [47].

Molecular dynamics

Force field settings The Materials Studio 4.4 package (Accelrys Software Inc., San Diego, CA, USA) was used (CINECA) to perform the MM and MD calculations through the Discover program using the implemented AMBER FF. The charges for each atom were either those implemented in the FF's file or those obtained through the charge equilibration method which were then scaled up by a factor of 1.414 ($\sqrt{2}$) [68]. The non-bond (NB) settings were different for the coulomb and the VdW interactions. For the vdW ones an atom-based summation method (cutoff = 15.50, spline width = 5.00 and buffer width = 2.00 Å) with a long range energy correction (tail correction = 15.50 Å) was used. For what concerns the electrostatic interactions, the dielectric value ε was set to 1.0, and the Ewald summation method (accuracy = 0.0001 kcal/mol and update width = 5.00 Å) was used. Finally, a scale factor of 1.3 was applied for the torsion interaction.

Protocols The MD simulations started from the energy-minimized structures. The PBC with NPT ensemble ($P = 0.0$ GPa and $T = 293$ K) were used for all the runs. In order to allow the cell to change both shape and volume, we used the Parrinello pressure control method [69], whereas Berendsen's thermostat with the default decay constant (0.01 ps) was used to control the temperature [70]. Transients of 3.5 ns were collected, after a 500 ps equilibration period, with 0.001 ps integration time and a sampling interval of 200 time-steps. The energy-optimized structures were obtained with the smart minimizer of the Discover module, satisfying a gradient of 0.1 kcal mol^{-1} $Å^{-1}$.

Modeling The structural models submitted to the simulations were generated on the basis of the single crystal X-ray structure (unit cells and atomic fractional coordinates) as reported in the cif file available as supplementary material. The periodic structural model was built by considering in the single unit cell the fractional parameters of each atom and allowing their $P2_12_12_1$ symmetry related images to be developed. This model was then converted to P1 by removing the symmetry constrains, in order to transform all the atomic positions into independent sites (four independent unit formulas in a unit cell with $a = 5.060$ Å; $b = 12.6478$ Å; $c = 28.567$ Å; $\alpha = \beta = \gamma = 90.0°$). The next modeling step was that of replicating this cell five times along the a axis and two times b axis, attaining in this way a super-cell of dimensions $a = 25.300$ Å; $b = 25.2956$ Å; $c = 28.567$ Å; $\alpha = \beta = \gamma = 90.0°$ with 40 independent units. No holonomic constraints have been used.

Molecular docking

Computational docking was carried out applying the Lamarckian genetic algorithm implemented in AutoDock 4.2.3 [71]. For fine docking we used the following parameters: grid spacing = 0.260 Å; number of runs = 100; npts = 70 70 70 centered on 6a, ga_num_evals = 25,000,000; ga_pop_size = 150 and ga_num_generations = 27,000. The graphical user interface AutoDockTools (1.5.6rc1, R45) [72] was used for establishing the Autogrid points as well as visualization of docked ligand-nucleic acid structures.

Supplementary information available

912822 is the CCDC number of the archived CIF file containing the supplementary crystallographic data refined and studied in this paper. These data are available free of charge

from the Cambridge Crystallographic Data Centre via http://www.ccdc.cam.ac.uk/data_request/cif or contacting the CCDC, 12 Union Road, Cambridge CB21EZ, UK.

References

1. Berridge MJ, Irvine RF (1989) Inositol phosphates and cell signaling. Nature 341(6239):197–205. doi:10.1038/341197a0
2. Billington DC (1993) Inositol phosphates: chemical synthesis and biological significance. VCH Verlagsgeselschaft; VCH Publishers, Weinheim
3. Sasaki K, Taylor IEP (1986) *Myo*-inositol synthesis from [1-H-3] glucose in *Phaseolus vulgaris* L during early stages of germination. Plant Physiol 81(2):493–496. doi:10.1104/Pp.81.2.493
4. Schmalz H-G, Wirth T (2003) Organic synthesis highlights. Wiley, Weinheim (Great Britain)
5. Larner J (2002) D-*chiro*-inositol—its functional role in insulin action and its deficit in insulin resistance. Int J Exp Diabetes Res 3(1):47–60
6. Iuorno MJ, Jakubowicz DJ, Baillargeon JP, Dillon P, Gunn RD, Allan G, Nestler JE (2002) Effects of D-*chiro*-inositol in lean women with the polycystic ovary syndrome. Endocr Pract 8(6):417–423
7. Sherman WR, Goodwin SL, Gunnell KD (1971) *Neo*-Inositol in mammalian tissues. Identification, measurement, and enzymatic synthesis from mannose 6-phosphate. Biochemistry (Mosc) 10(19):3491–3499
8. Martin JB, Laussmann T, Bakker-Grunwald T, Vogel G, Klein G (2000) *neo*-Inositol polyphosphates in the amoeba *Entamoeba histolytica*. J Biol Chem 275(14):10134–10140
9. Shapiro J, Belmaker RH, Biegon A, Seker A, Agam G (2000) *Scyllo*-inositol in post-mortem brain of bipolar, unipolar and schizophrenic patients. J Neural Transm 107(5):603–607
10. Ichimura K, Kohata K, Yamaguchi Y, Douzono M, Ikeda H, Koketsu M (2000) Identification of L-inositol and scyllitol and their distribution in various organs in chrysanthemum. Biosci Biotechnol Biochem 64(4):865–868
11. Shaldubina A, Ju S, Vaden DL, Ding D, Belmaker RH, Greenberg ML (2002) *Epi*-inositol regulates expression of the yeast INO1 gene encoding inositol-1-P synthase. Mol Psychiatry 7(2):174–180. doi:10.1038/sj.mp.4000965
12. Williams RS, Cheng L, Mudge AW, Harwood AJ (2002) A common mechanism of action for three mood-stabilizing drugs. Nature 417(6886):292–295. doi:10.1038/417292a
13. Sherman WR, Stewart MA, Kurien MM, Goodwin SL (1968) The measurement of *myo*-inositol, *myo*-inosose-2 and *scyllo*-inositol in mammalian tissues. Biochim Biophys Acta 158(2):197–205
14. Horner WH, Thaker IH (1968) The metabolism of *scyllo*-inositol in *Streptomyces griseus*. Biochim Biophys Acta 165(2):306–308
15. Kiely DE, Fletcher HG Jr (1969) Cyclization of D-*xylo*-hexos-5-ulose, a chemical synthesis of *scyllo*-and *myo*-inositols from D-glucose. J Org Chem 34(5):1386–1390
16. Nitz M, Fenili D, Darabie AA, Wu L, Cousins JE, McLaurin J (2008) Modulation of amyloid-β aggregation and toxicity by inosose stereoisomers. FEBS J 275(8):1663–1674. doi:10.1111/j.1742-4658.2008.06321.x
17. Barili PL, Berti G, Catelani G, Dandrea F (1992) New synthetic pathways to 5-*C*-alkoxypyranosides and to hexos-5-ulose derivatives. Gazz Chim Ital 122(4):135–142
18. Catelani G, Corsaro A, D'Andrea F, Mariani M, Pistarà V, Vittorino E (2003) Convenient preparation of L-*arabino*-hexos-5-ulose derivatives from lactose. Carbohydr Res 338(22):2349–2358. doi:10.1016/j.carres.2003.08.001
19. Catelani G, D'Andrea F, Guazzelli L, Pistarà V (2009) Toward the synthesis of fine chemicals from lactose: preparation of D-*xylo* and L-*lyxo*-aldohexos-5-ulose derivatives. Carbohydr Res 344(6):717–724. doi:10.1016/j.carres.2009.01.014
20. Corsaro A, Catelani G, D'Andrea F, Fisichella S, Mariani M, Pistarà V (2003) A new route for the chemical valorisation of lactose. Environ Sci Pollut Res 10(5):325–328. doi:10.1065/espr2001.12.104.2
21. Pistarà V, Chiacchio MA, Corsaro A (2010) Towards the synthesis of new dideoxy δ-dicarbonyl heptoses. Carbohydr Res 345(10):1482–1485. doi:10.1016/j.carres.2010.03.013
22. Corsaro A, Pistarà V, Catelani G, D'Andrea F, Adamo R, Chiacchio MA (2006) A new method for the synthesis of carba-sugar enones (gabosines) using a mercury(II)-mediated opening of 4,5-cyclopropanated pyranosides as the key-step. Tetrahedron Lett 47(37):6591–6594. doi:10.1016/j.tetlet.2006.07.023
23. Pistarà V, Barili PL, Catelani G, Corsaro A, D'Andrea F, Fisichella S (2000) A new highly diastereoselective synthesis of *epi*-inositol from D-galactose. Tetrahedron Lett 41(17):3253–3256. doi:10.1016/S0040-4039(00)00360-9
24. Catelani G, Corsaro A, D'Andrea F, Mariani M, Pistarà V (2002) Intramolecular aldol cyclization of l-lyxo-hexos-5-ulose derivatives: a new diastereoselective synthesis of d-chiro-inositol. Bioorg Med Chem Lett 12(22):3313–3315. doi:10.1016/S0960-894x(02)00692-3
25. Pistarà V, Rescifina A, Punzo F, Greco G, Barbera V, Corsaro A (2011) Design, synthesis, molecular docking and crystal structure prediction of new azasugar analogues of α-glucosidase inhibitors. Eur J Org Chem 36:7278–7287. doi:10.1002/ejoc.201100832
26. Alberti G, Lombardo GM, Pappalardo GC, Vivani R (2002) Modeling and analysis of the X-ray powder diffraction structure of gamma-zirconium phosphates pillared with butyl chains through molecular dynamics simulations. Chem Mater 14(1):295–303. doi:10.1021/Cm011156g
27. Caminiti R, Gleria M, Lipkowitz KB, Lombardo GM, Pappalardo GC (1997) Molecular dynamics simulations combined with large angle X-ray scattering technique for the determination of the structure, conformation, and conformational dynamics of polyphosphazenes in amorphous phase: study of poly[di(4-methylphenoxy)phosphazene]. J Am Chem Soc 119(9):2196–2204
28. Carriedo GA, Alonso FJG, Alvarez JLG, Lombardo GM, Pappalardo GC, Punzo F (2004) Molecular dynamics (MD) simulations and large-angle X-ray scattering (LAXS) studies of the solid-state structure and assembly of isotactic (R)-poly(2,2′-dioxy-1,1′-binaphthyl-)phosphazene in the bulk state and in the cast film. Chem Eur J 10(15):3775–3782. doi:10.1002/chem.200400051
29. Lombardo GM, Pappalardo GC (2008) Thermal effects on mixed metal (Zn/Al) layered double hydroxides: direct modeling of the X-ray powder diffraction line shape through molecular dynamics simulations. Chem Mater 20(17):5585–5592. doi:10.1021/Cm801053d
30. Lombardo GM, Pappalardo GC, Punzo F, Costantino F, Costantino U, Sisani M (2005) A novel integrated X-ray powder diffraction (XRPD) and molecular dynamics (MD) approach for modelling mixed-metal (Zn, Al) layered double hydroxides (LDHs). Eur J Inorg Chem 24:5026–5034. doi:10.1002/ejic.200500666
31. Cremer D, Pople JA (1975) General definition of ring puckering coordinates. J Am Chem Soc 97:1354–1358. doi:10.1021/ja00839a011
32. Alvarez JLG, Amato ME, Lombardo GM, Carriedo GA, Punzo F (2010) Self-organization by chiral recognition based on ad hoc chiral pockets in cyclotriphosphazenes with binaphthoxy and biphenoxy substituents: an X-ray, NMR and computational study. Eur J Inorg Chem 28:4483–4491. doi:10.1002/ejic.201000586

33. Evans DG, Boeyens JCA (1989) Conformational-analysis of ring pucker. Acta Crystallogr B 45:581–590. doi:10.1107/S0108768189008190
34. Desiraju GR, Steiner T (1999) The weak hydrogen bond in structural chemistry and biology. international union of crystallography monographs on crystallography, vol 9. Oxford University Press, Oxford
35. Steiner T (1996) C–H···O hydrogen bonding in crystals. Crystallogr Rev 6:1–51. doi:10.1080/08893119608035394
36. Jeffrey GA, Maluszynska H, Mitra J (1985) Hydrogen-bonding in nucleosides and nucleotides. Int J Biol Macromol 7(6):336–348. doi:10.1016/0141-8130(85)90048-0
37. Dinadayalane TC, Leszczynski J (2009) Geometries and stabilities of various configurations of benzene dimer: details of novel V-shaped structure revealed. Struct Chem 20(1):11–20. doi:10.1007/s11224-009-9411-6
38. DiStasio RA, von Helden G, Steele RP, Head-Gordon M (2007) On the T-shaped structures of the benzene dimer. Chem Phys Lett 437(4–6):277–283. doi:10.1016/j.cplett.2007.02.034
39. Fraga ARL, Destri GL, Forte G, Rescifina A, Punzo F (2010) Could *N*-(diethylcarbamothioyl)benzamide be a good ionophore for sensor membranes? J Mol Struct 981(1–3):86–92
40. Grimme S (2008) Do special noncovalent pi–pi stacking interactions really exist? Angew Chem Int Ed 47(18):3430–3434. doi:10.1002/anie.200705157
41. Sato T, Tsuneda T, Hirao K (2005) A density-functional study on pi–aromatic interaction: benzene dimer and naphthalene dimer. J Chem Phys 123(10):104307. doi:10.1063/1.2011396
42. Kitaĭgorodskiĭ AI (1973) Molecular crystals and molecules. Physical chemistry, a series of monographs, vol 29. Academic Press, New York
43. Burden CJ, Oakley AJ (2007) Anisotropic atomic motions in high-resolution protein crystallography molecular dynamics simulations. Phys Biol 4(2):79–90. doi:10.1088/1478-3975/4/2/002
44. Car R, Parrinello M (1985) Unified approach for molecular-dynamics and density-functional theory. Phys Rev Lett 55(22): 2471–2474
45. Hobza P, Sponer J (1999) Structure, energetics, and dynamics of the nucleic acid base pairs: nonempirical ab initio calculations. Chem Rev 99(11):3247–3276
46. Lombardo GM, Portalone G, Chiacchio U, Rescifina A, Punzo F (2012) Potassium caffeate/caffeic acid co-crystal: the rat race between the catecholic and carboxylic moieties in an atypical co-crystal. Dalton Trans 41(47):14337–14344. doi:10.1039/c2dt31092a
47. Lombardo GM, Portalone G, Colapietro M, Rescifina A, Punzo F (2011) From the X-rays to a reliable "low cost" computational structure of caffeic acid: dFT, MP2, HF and integrated molecular dynamics-X-ray diffraction approach to condensed phases. J Mol Struct 994(1–3):87–96. doi:10.1016/j.molstruc.2011.03.001
48. Cornell WD, Cieplak P, Bayly CI, Gould IR, Merz KM, Ferguson DM, Spellmeyer DC, Fox T, Caldwell JW, Kollman PA (1995) A 2nd generation force-field for the simulation of proteins, nucleic-acids, and organic-molecules. J Am Chem Soc 117(19):5179–5197
49. Reilly AM, Habershon S, Morrison CA, Rankin DW (2010) Simulating thermal motion in crystalline phase-I ammonia. J Chem Phys 132(13):134511. doi:10.1063/1.3387952
50. Reilly AM, Wann DA, Morrison CA, Rankin DWH (2007) Experimental equilibrium crystal structures: molecular dynamics as a probe for atomic probability density functions. Chem Phys Lett 448(1–3):61–64. doi:10.1016/j.cplett.2007.09.073
51. Falshaw A, Hart JB, Tyler PC (2000) New syntheses of 1D-and 1L–1, 2-anhydro-myo-inositol and assessment of their glycosidase inhibitory activities. Carbohydr Res 329(2):301–308. doi:10.1016/S0008-6215(00)00192-0
52. Freeman S, Hudlicky T (2004) New oligomers of conduritol-F and muco-inositol, synthesis and biological evaluation as glycosidase inhibitors. Bioorg Med Chem Lett 14(5):1209–1212. doi:10.1016/j.bmcl.2003.12.050
53. Painter GF, Eldridge PJ, Falshaw A (2004) Syntheses of tetrahydroxyazepanes from chiro-inositols and their evaluation as glycosidase inhibitors. Bioorg Med Chem 12(1):225–232. doi:10.1016/j.bmc.2003.10.003
54. Paul BJ, Willis J, Martinot TA, Ghiviriga I, Abboud KA, Hudlicky T (2002) Synthesis, structure, and biological evaluation of novel N- and O-linked diinositols. J Am Chem Soc 124(35): 10416–10426. doi:10.1021/Ja0205378
55. Sun M, Wang T, Shu X (2009) The use of inositol derivative or salts thereof in the manufacture of medicaments as glycosidase inhibitors or medicaments for treating diabetes. WO200915 5753(A1), 30 Dec 2009
56. Sureshan KM, Ikeda K, Asano N, Watanabe Y (2008) Efficient syntheses of optically pure chiro- and allo-inositol derivatives, azidocyclitols and aminocyclitols from myo-inositol. Tetrahedron 64(18):4072–4080. doi:10.1016/j.tet.2008.02.032
57. Sim L, Jayakanthan K, Mohan S, Nasi R, Johnston BD, Pinto BM, Rose DR (2010) New Glucosidase inhibitors from an ayurvedic herbal treatment for type 2 diabetes: structures and inhibition of human intestinal maltase-glucoamylase with compounds from *Salacia reticulata*. Biochemistry (Mosc) 49(3): 443–451. doi:10.1021/Bi9016457
58. http://www.rcsb.org/PDBcode 3L4W
59. Mazue F, Colin D, Gobbo J, Wegner M, Rescifina A, Spatafora C, Fasseur D, Delmas D, Meunier P, Tringali C, Latruffe N (2010) Structural determinants of resveratrol for cell proliferation inhibition potency: experimental and docking studies of new analogs. Eur J Med Chem 45(7):2972–2980. doi:10.1016/j.ejmech.2010.03.024
60. de Melo EB, Gomes AD, Carvalho I (2006) Alpha- and beta-glucosidase inhibitors: chemical structure and biological activity. Tetrahedron 62(44):10277–10302. doi:10.1016/j.tet.2006.08.055
61. Wallace AC, Laskowski RA, Thornton JM (1995) Ligplot: a program to generate schematic diagrams of protein ligand interactions. Protein Eng 8(2):127–134. doi:10.1093/protein/8.2.127
62. Perrin DD, Armarego WLF, Perrin DR (1980) Purification of laboratory chemicals, 2nd edn. Pergamon Press, Oxford
63. Hirshfeld FL (1976) Can X-ray data distinguish bonding effects from vibrational smearing? Acta Crystallogr a 2:239–244. doi:10.1107/s0567739476000533
64. Vandersluis P, Spek AL (1990) Bypass: an effective method for the refinement of crystal-structures containing disordered solvent regions. Acta Crystallogr A 46:194–201. doi:10.1107/S0108767389011189
65. Bruker (2007) SAINT-Plus. Bruker AXS Inc, Madison
66. Bruker (2001) SADABS. Bruker AXS Inc, Madison
67. Macrae CF, Edgington PR, McCabe P, Pidcock E, Shields GP, Taylor R, Towler M, van De Streek J (2006) Mercury: visualization and analysis of crystal structures. J Appl Crystallogr 39:453–457. doi:10.1107/S002188980600731x
68. Rappe AK, Goddard WA (1991) Charge equilibration for molecular-dynamics simulations. J Phys Chem 95(8):3358–3363. doi:10.1021/J100161a070
69. Parrinello M, Rahman A (1982) Strain fluctuations and elastic constants. J Chem Phys 76:2662–2666
70. Berendsen HJC, Postma JPM, van Gunsteren WF, DiNola A, Haak JR (1984) Molecular dynamics with coupling to an external bath. J Chem Phys 81:3684–3690
71. Morris GM, Goodsell DS, Halliday RS, Huey R, Hart WE, Belew RK, Olson AJ (1998) Automated docking using a Lamarckian genetic algorithm and an empirical binding free energy function. J Comput Chem 19(14):1639–1662. doi:10.1002/(Sici)1096-987x(19981115)19:14<1639:Aid-Jcc10>3.0.Co;2-B
72. Sanner MF (1999) Python: a programming language for software integration and development. J Mol Graph Model 17(1):57–61